In vivo urinary compatibility of Mg-Sr-Ag alloy in swine model

Tie, Di; Hort, Norbert; Chen, Minfang; Guan, Renguo; Ulasevich, Sviatlana; Skorb, Ekaterina V.; Zhao, Dapeng; Liu, Yili; Holt-Torres, Patricia; Liu, Huinan

Published in:
Bioactive Materials

DOI:
10.1016/j.bioactmat.2021.05.046

Publication date:
2022

Document Version
Publisher's PDF, also known as Version of record

Bioactive Materials 7 (2022) 254–262

Contents lists available at ScienceDirect

Bioactive Materials

journal homepage: www.sciencedirect.com/journal/bioactive-materials

In vivo urinary compatibility of Mg-Sr-Ag alloy in swine model

Di Tie [a], Norbert Hort [b], Minfang Chen [c], Renguo Guan [a], Sviatlana Ulasevich [d], Ekaterina V. Skorb [d], Dapeng Zhao [e,*], Yili Liu [f], Patricia Holt-Torres [g], Huinan Liu [g]

[a] Engineering Research Center of Continuous Extrusion, Ministry of Education, Dalian Jiaotong University, Dalian, 116028, China
[b] Magnesium Innovation Center, Helmholtz-Zentrum Geesthacht, D-21502, Geesthacht, Germany
[c] School of Materials Science and Engineering, Tianjin University of Technology, Tianjin, 300384, China
[d] Infochemistry Scientific Center, ITMO University, St. Petersburg, 192007, Russia
[e] College of Biology, Hunan University, 410082, Changsha, China
[f] Department of Urology, China Medical University, Shenyang, 110084, China
[g] Department of Bioengineering, Bourns College of Engineering, University of California at Riverside, CA, 92521, USA

ARTICLE INFO

Keywords:
In vivo
Magnesium alloy
Biodegradable metals
Mechanical properties
Urinary compatibility

ABSTRACT

A biodegradable metallic ureteral stent with suitable mechanical properties and antibacterial activity remains a challenge. Here we reveal the scientific significance of a biodegradable Mg-Sr-Ag alloy with a favorable combination of balanced mechanical properties, adjustable indwelling time in urinary tract and evident antibacterial activity via *in vivo* experiments in a swine model. Attributed to the rheo-solidification process, equiaxial microstructure and significantly refined grains (average grain size: 27.1 μm) were achieved. $Mg_{17}Sr_2$ and Mg_4Ag were found as the primary precipitates in the matrix, due to which the alloy obtained ca. 111% increase in ultimate tensile strength in comparison to pure magnesium. Both the *in vitro* and *in vivo* results demonstrated the satisfactory biocompatibility of the alloy. Histological evaluation and bioindicators analysis suggested that there was no tissue damage, inflammation and lesions in the urinary system caused by the degradation process. The stent also improved the post-operative bladder functions viewed from the urodynamic results. Our findings highlight the potential of this alloy as antibacterial biodegradable urinary implant material.

1. Introduction

As a common obstructive uropathy, ureteric obstruction is usually caused by extrinsic compression [1,2]. The primary objective of ureteric obstruction treatment is to optimize renal functions and relieve symptoms [2,3]. Traditional therapeutic methods include open endourological surgeries and minimally invasive techniques, while stenting has been becoming the preferred current management [1,4,5]. A ureteral stent is an implant to drain the upper urinary tract and facilitate the ureteral reconstruction when the ureter is obstructed [2,4]. Polymers are the most widely used traditional materials for the manufacture of ureteral stents, especially the double-J stents, in which are especially suitable for short term treatment. However, frequent replacement is necessary to prevent various complications, including encrustation, peri-infections, recurrent stenosis and even tumor ingrowth [6,7]. Compared to polymer based ureteral implant materials, metallic materials has higher inherent antibacterial activity and better mechanical performance [8]. Because polymer ureteral implant materials are prone to bacterial infection, current polymer stents are intended for short dowelling time in urinary tract [9]. Frequent replacement is necessary to prevent various complications, including encrustation, peri-infections, recurrent stenosis and even tumor ingrowth [6]. Therefore, metallic ureteral stents are developed to reduce exchange frequency, maintain better lumen patency and prevent complications [6,10]. In recent years, metallic ureteral stents are more frequently applied as a first-line therapy, or in case of failure of traditional approaches. Several metallic ureteral stents have been clinically used including Memokath™, Resonance™, Uventa™, *etc* [6]. Unlike polymer stents, metallic stents have higher mechanical properties and longer service lives. However, infections and bacteriuria due to biofilm formation cannot be avoided during the long period of implantation [11,12].

To traditional ureteral stents, the constant surface will inevitably be covered by biofilm, which has been reported as the first step in the process of peri-implant infection [4,13,14]. According to Beysens' study,

Peer review under responsibility of KeAi Communications Co., Ltd.
* Corresponding author.
E-mail address: dpzhao@hnu.edu.cn (D. Zhao).

https://doi.org/10.1016/j.bioactmat.2021.05.046
Received 25 October 2020; Received in revised form 23 April 2021; Accepted 26 May 2021
Available online 4 June 2021

bacterial colonization on biofilm was found in 24% cases in the first 4 weeks post-operation and more than 70% after 6 weeks [4]. Furthermore, previous studies also reported on diabetes mellitus and chronic renal failure associated with peri-implant infections [12]. Routine treatment were proved not effective to prevent these complications. For example, a long-term antibiotic treatment throughout the entire implantation period was reported by Akay et al. [13], while no significant remission of infections was observed. Indwelling time was proved the most crucial parameter to determine the biofilm formation on stents [15]. Therefore, biodegradable stents are gaining increasing research interest duo to their natural advantage of constantly degrading surface, which are immune to biofilm formation [16–18]. Like the other two commonly studied biodegradable metallic materials, iron and zinc, magnesium and its alloys also have inherent antimicrobial activities [8,19,20]. Lock et al. [21] identified a significant decrease in bacterial proliferation when magnesium alloys degraded in artificial urine, and similar phenomena were also reported by Zhang et al. [22]. Thus, the evident antibacterial activity makes magnesium alloy a very favorable candidate as biodegradable ureteral implant material.

Previously, we have preliminarily validated the applicability of manufacturing biodegradable bone fixation device by a Mg-Sr alloy [23]. We also have demonstrated the evident antibacterial activity of biodegradable silver containing magnesium alloys *in vitro* [17]. Mg-Sr alloys have favorable mechanical properties and osteogenic activity, and therefore is especially suitable for bone fracture fixation as we specified in our previous publication. However, when using in ureteral circumstance, Mg-Sr alloy's corrosion rate cannot be widely adjusted. Therefore, we developed Mg-Sr-Ag alloy to obtain better degradable property, as well as stronger antibacterial activity. By combining the outstanding mechanical properties of Mg-Sr alloy with the evident antibacterial activity of silver content, we designed an innovative Mg-1.0Sr-0.5Ag (wt.%) alloy. We intensively studied the biocompatibility of the alloy, especially its impact on urinary system and urodynamics. The role of local ion release in the inhibition to peri-implant infections is also focused on in this study.

2. Materials and methods

Mg-1.0Sr-0.5Ag (wt.%) alloy was fabricated by semi-solid rheo-extrusion, whose scheme and processing mechanism were specified in our previous studies [24,25]. The alloy was nominated as JQ alloy according to ASTM standard, in which J stands for strontium and Q stands for silver [26]. An optical microscope (LV150, Nikon, Tokyo, Japan) was utilized for the observation on the microstructure. An X-ray diffractometer (XRD; Siemens-D5000, Muenchen, Germany) with Cu Kα1 radiation (k = 0.154 nm) was employed for phase identification. Radiographs of the implantation site was collected by using an X-ray system (Mednova, Hangzhou, China) with a standard imaging module. The surface morphology was observed by a scanning electron microscope (SEM; Shimadzu, Kyoto, Japan) fitted with EDS (energy dispersive X-ray spectrometer, Ametek, NJ, USA) was employed for the surface composition analysis. An XPS (X-ray induced photoelectron spectroscope, Shimadzu, Manchester, UK) was utilized for identification of the chemical compositions of the surface layer. A mechanical tester (CMT5300, MST inc., China) was employed for the tensile tests, with a tensile rate of 1.0×10^{-3} s^{-1}. The morphology of fractured surface and longitudinal sections were observed by SEM.

The *in vitro* cytotoxicity of JQ alloy was determined by co-culture with human primary cells. Human LO2 cells (human normal liver cells) were extracted and cultured in cell culture medium (Sigma Aldrich, Taufkirchen, Germany) plus 10 vol% fetal bovine serum (FBS; Linz, Austria). A fluorescence microscope (Eclipse, Nikon, Duesseldorf, Germany) was used to determine the cell viability via a Live/Dead staining kit (Invitrogen, Karlsruhe, Germany) according to the instructions. A Cell Counting Kit (CCK-8; Meilun Bio, Liaoning, China) was used for characterization of cell proliferation. Hemolysis tests were carried out by measuring the hemoglobin content using a spectrophotometer (Unico, Wisconsin, USA) following the ISO 10993 standard.

The experimental animals, *Bama Minipigs* were provided by NTG Hospital, Shenyang. There were three animals stented by pure magnesium (Mg) implants as the control group, and the other three animals stented by JQ implants as the test group. All the operations strictly followed the related national regulations and were approved by the local animal welfare committee. To comprehensively determine the potential toxicity to urinary system from the degradation products, tissue sections of the renal tubules, the renal pelvis, the ureter and the bladder were collected and hematoxylin/eosin stained for histological evaluation after 12 weeks implantation by using biomicroscopy (Olympus, Tokyo, Japan). Bladder urodynamics were evaluated in the both experimental groups using an automatic urodynamics analyzer (Potent, Guangzhou, China) with conscious unrestrained cystometry method. Bacteriuria was examined via agar diffusion methods (Forthrightbio, Shanghai, China) and expressed as CFU (colony forming units) per milliliter. The cellular morphology of the transitional epithelium cells after implantation was observed using a transmission electron microscope (TEM; Jeol, Mitaka, Japan).

In vitro and blood tests were performed in six duplicates, and urine tests were performed in four duplicates. All the statistical results are presented in the form of mean value ± standard deviation. The difference of results between different groups were compared by one-way analysis of variance test. The confidence levels are 95.0% (*: $p < 0.05$) and 99.0% (**: $p < 0.01$); no significant difference ($p \geq 0.05$) was presented with 'NS'.

3. Results

3.1. Material characterization and degradation behavior

The microstructure of JQ alloy is displayed Fig. 1a, in which the equiaxed grains due to the rheo-solidification can be evidently observed. During the rheo-solidificaiton process, primary α-Mg matrix solidified first under the coupling fields composed of cooling field and vibration field, which fully spheroidized and refined the grains [24]. As a result, the alloy matrix was mainly composed of spherical equiaxed grains with the average size of 27.1 μm. The peaks at 63.5°, 68.9° and 70.3° in the XRD diffraction pattern (Fig. 1b) could be indexed as the signal of $Mg_{17}Sr_2$, which was also found in Mg-Sr binary alloy in our previous study [27]. Only small amount of Mg_4Ag was observed in the alloy, indicating that most of the silver content was dissolved in the magnesium matrix. Radiographic analysis of the implantation site showed that the stent maintained its integrity until the end of the study (Fig. 1c). The EDS line scan results in Fig. 1d present the linear distribution of Mg, Sr and Ag on the surface of the test alloy at 12w post-operation. The concentration of magnesium, strontium and silver in the corrosion layer all decreased to very low levels at ca. 30 μm of the scanning line (Fig. 1d), which corresponded to grain boundary according to the SEM image of surface morphology. Attributed to the rheo-solidification process, the grain boundaries composed of secondary solid phases had higher concentration of strontium and silver than the interior of grains composed of primary solid phases [23]. As a result, the interior of grains showed more negative corrosion potential than grain boundaries, so the grain boundaries constituted cathodic network in electrochemical corrosion [23]. Thus, the anodic areas were separated and the corrosion process was limited and homogenized.

XPS analysis towards the implants (Fig. 2) was carried out to identify the degradation products. The Mg 2p spectra stretched out between 47 eV and 53 eV, and could be identified as MgO at 50.3 eV and $Mg(OH)_2$ at 49.5 eV. $Mg(OH)_2$ is the primary corrosion product when magnesium alloy contacts with aqueous solutions, while the appearance of MgO was due to reversible dehydration of $Mg(OH)_2$ in the corrosion layer [17]. The species of degradation products present in the corrosion layer after implantation were identified by XPS analysis and their atomic

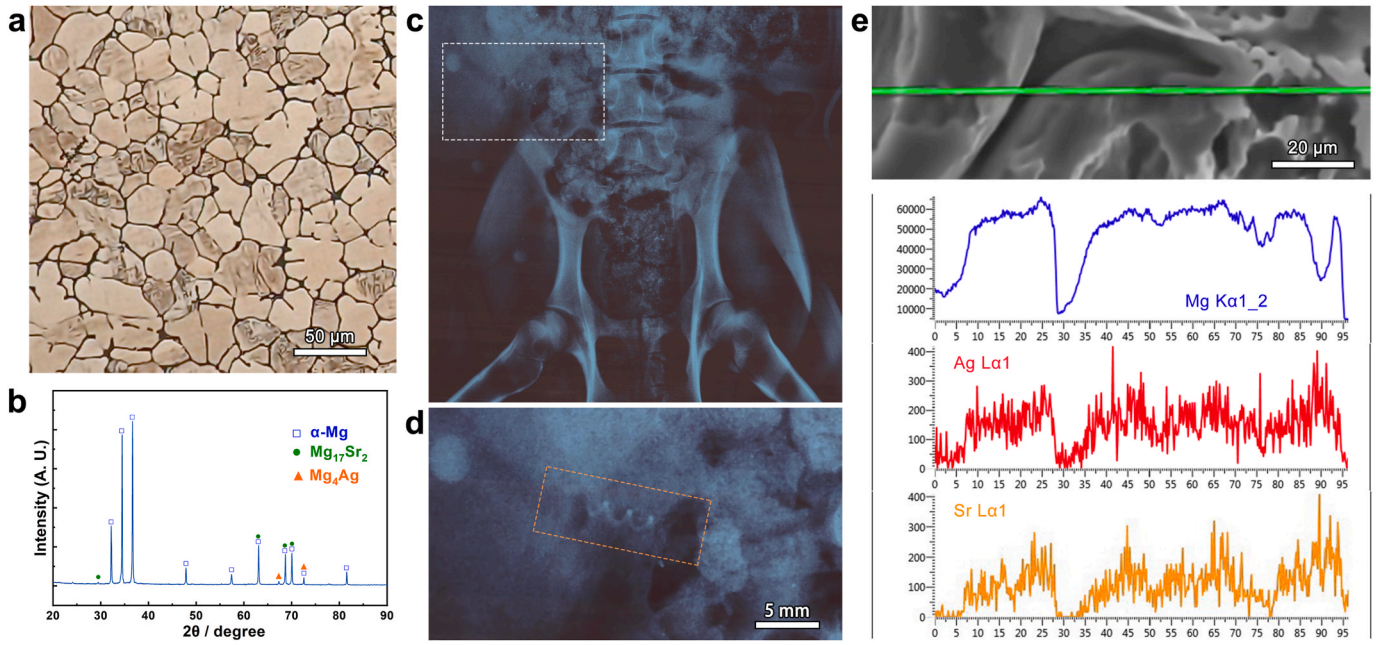

Fig. 1. Optical micrograph (**a**) and XRD analysis results (**b**) of JQ alloy; radiographic observation on the implant site (**c**) and the stent (**d**); EDS line scan results of the surface layer of the alloy at 12w post-operation (**e**).

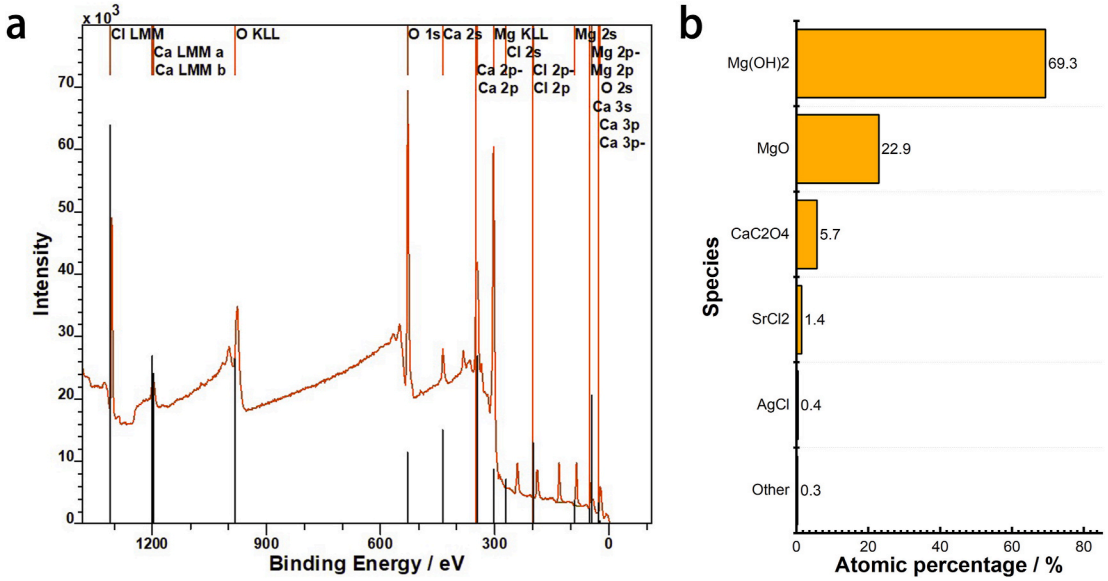

Fig. 2. XPS survey spectra of the corrosion products after 8 weeks implantation (**a**) and the chemical composition of the corrosion products (**b**).

compositions were calculated via the signal integration (Fig. 2b). Apart from the large amount of $Mg(OH)_2$ and MgO, the corrosion layer also contain 5.7 at.% of CaC_2O_4 and small amount of $SrCl_2$, AgCl and other compounds.

Fig. 3 shows the engineering stress-strain curves of pure magnesium and JQ alloy at room temperature. The grain refinement effect brought by rheo-solidification led to evident grain refinement strengthening effect, due to which both the tensile strength and the elongation of JQ alloy also showed pronounced increases. Compared to pure magnesium (105.9 MPa), the JQ alloy obtained ca. 111% increase in ultimate tensile strength (223.7 MPa). A stress plateau could be observed at the onset of plastic deformation of pure magnesium due to profuse twinning [28]. Fig. 3 also depicts a 3D rendering in SEM micrograph of the initial microstructure of JQ alloy. The initial microstructure of JQ exhibits a majority of equiaxed grains with small amount of dispersed second phase particles. Under uniaxial loading, pure magnesium exhibited a mixture of cleavage fracture and intergranular fracture. On the contrary, denser and deeper dimples were observed in JQ alloy, hinting that the alloy underwent ductile failure. Therefore, the JQ sample displayed ductile fracture morphology including less quasi-cleavage planes whilst more dimples and tear ridges (Fig. 3).

3.2. Cellular compatibility and physiological indices

The results for fluorescence analysis of LO2 cells seeded on Mg and JQ both showed normal morphology in fusiform shape (Fig. 4). The nucleus, the cellular membrane, and the mitochondria displayed their regular morphology, indicating the normal cellular colonization and

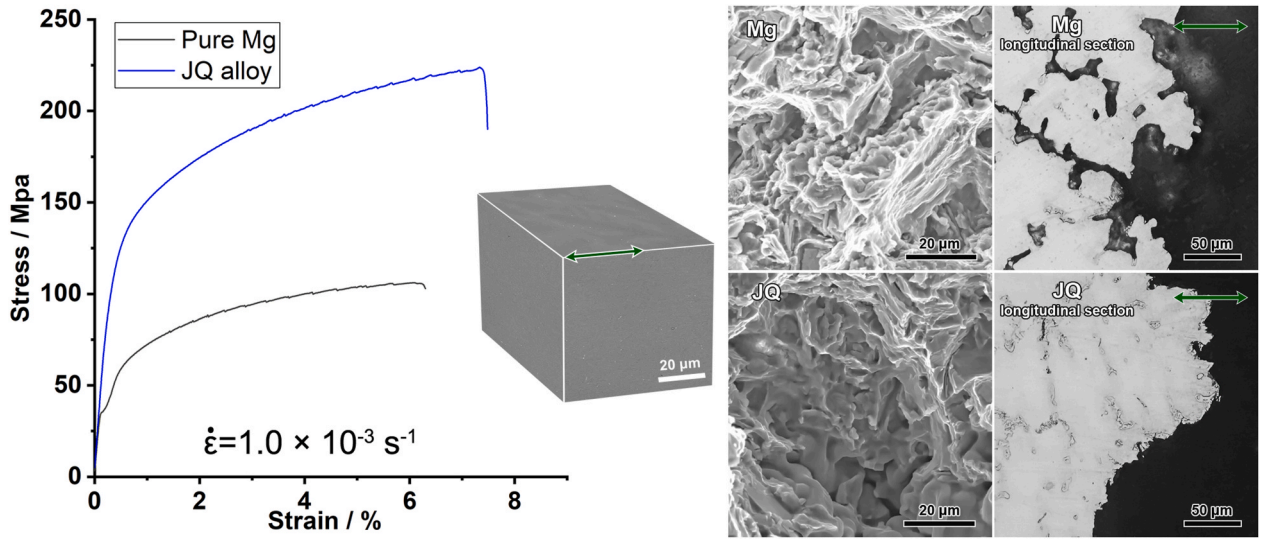

Fig. 3. Stress versus strain response of Mg and JQ, 3D reconstructed SEM image of JQ alloy's initial microstructure and the fracture morphology of the tensile samples; the double arrowheads stand for load direction.

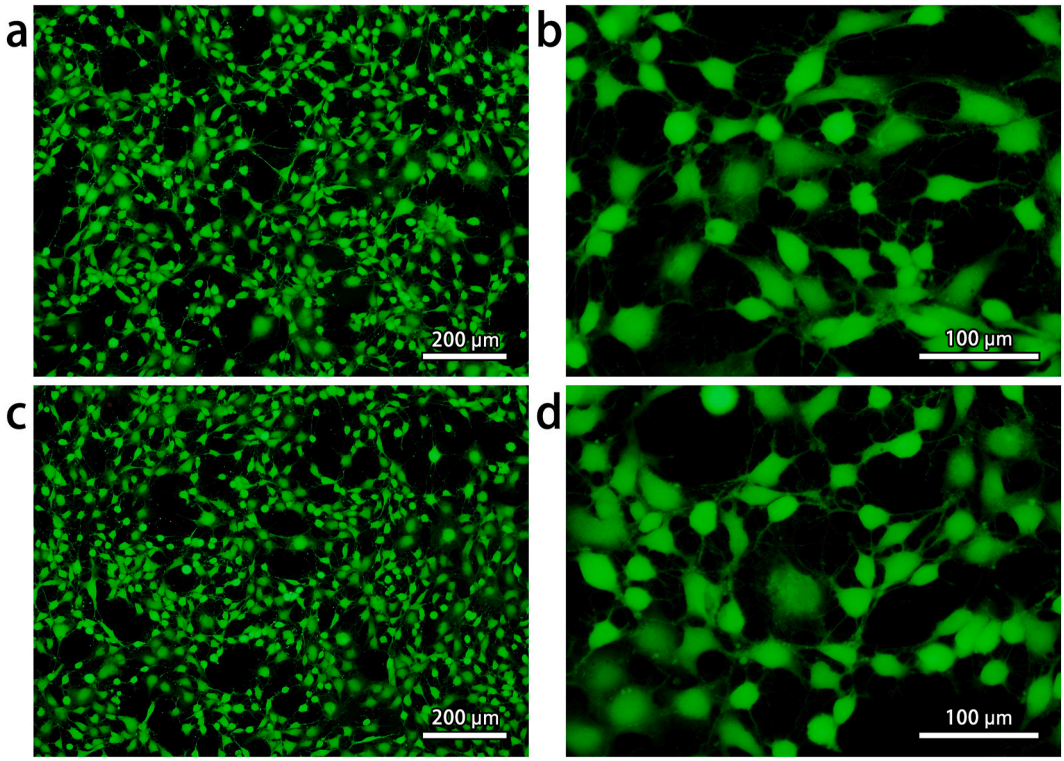

Fig. 4. Fluorescent microscopy images of the human normal liver cells seeded on Mg samples (**a, b**) and JQ samples (**c, d**); the cells were stained in green (live cells) or in red (dead cells).

proliferation on the surface of JQ alloy. After 4 days culture, there were very few dead cells on the surface of JQ alloy (Fig. 4c). The CCK-8 results showed no significant difference ($p > 0.05$) between the LO2 cell proliferation rate in JQ group (146.1% ± 15.0%) and in Mg group (152.3% ± 15.9%) (Fig. 5). The *in vitro* cytocompatibility results demonstrated that JQ alloy has equivalent cellular compatibility with pure magnesium.

The hemolysis results (Fig. 6a) showed that pure magnesium induced a 5.3% ± 1.0% hemolysis, whilst the hemolysis percentage in JQ group was 5.7% ± 1.4%. The hemolysis results of the two groups exhibited no significant difference, indicating that JQ alloy had a similar hemocompatibility with pure magnesium, which has been proved a non-toxic implant material [29]. Three crucial biochemical indices were analyzed via blood tests and summarized in Fig. 6b–d. Low level of albumin was found in both magnesium and JQ groups (Fig. 6b), which clearly demonstrated that no peri-implant infections occurred during implantation period [30]. There was no significant difference ($p > 0.05$) between the serum α-HBDH concentration at 0w and 6w (Fig. 6c), which is a primary indicator of cardiac functions. Higher expressions of serum ALT/AST rate in JQ group were observed on the first week of implantation, and recovered to the same level as the magnesium group on the sixth week (Fig. 6d). Given ALT/AST ratio is a sensitive predictor of liver

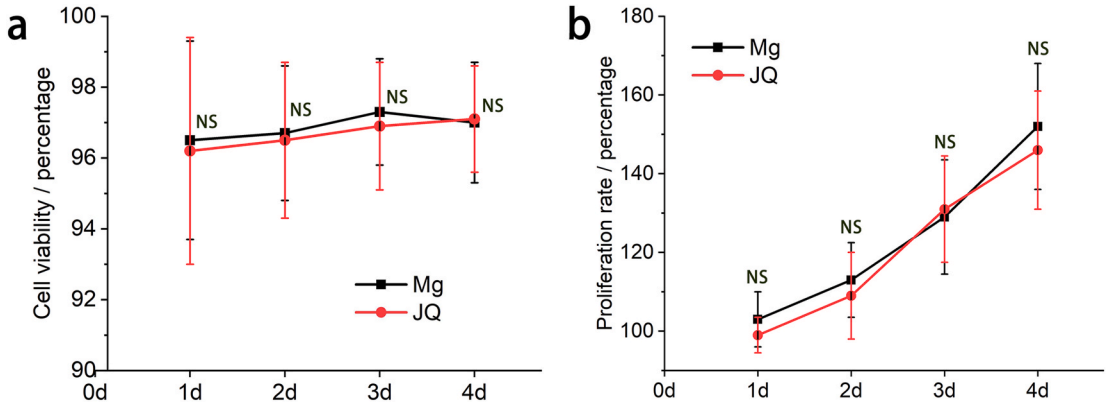

Fig. 5. CCK-8 results of the cell viability (**a**) and the proliferation rate (**b**) of the human normal liver cells seeded on pure magnesium and JQ alloy.

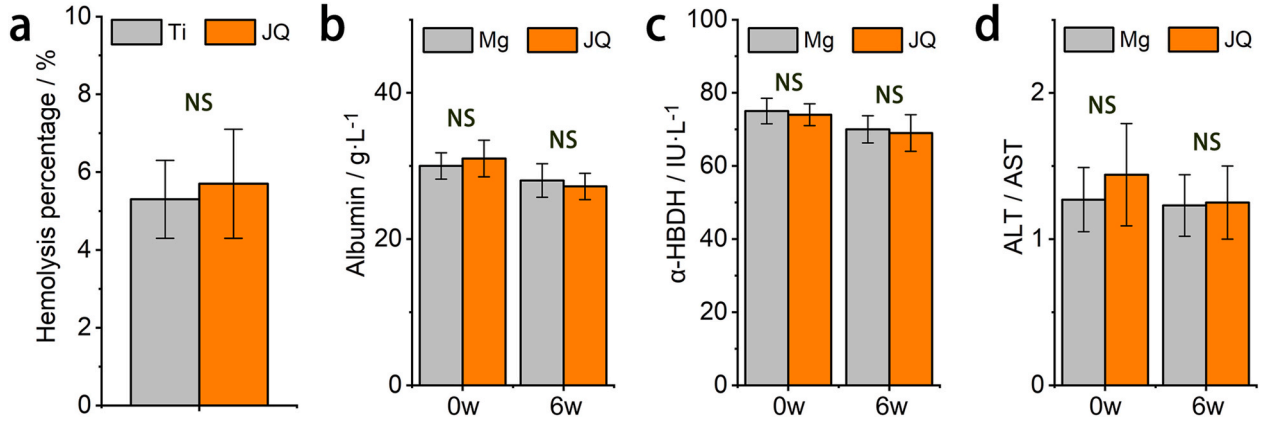

Fig. 6. The hemolysis results (**a**), serum albumin level (**b**), serum concentration of α-HBDH (**c**) and serum ALT/AST rate (**d**) of the animals in control and test groups.

damage, the results demonstrate that the degradation process did not significantly affect the liver functions [31].

3.3. Urinary compatibility

To comprehensively access the potential toxicity to urinary system induced by the degradation process at 12w post-operation, tissue sections of the renal tubules, the renal pelvis, the ureter and the bladder were collected for histological evaluation (Fig. 7).

Inflammation and tissue lesions caused by potential toxic exposure were specifically focused on. Absence of necrotic tissue and similar cellular structures were observed in both magnesium and JQ groups. Tissue from the renal tubules displayed neither evident morphological changes nor hydropic degeneration in proximal tubule and medullary loop (Fig. 7a). Assessment of the renal pelvis sections also showed no pathological changes or inflammation (Fig. 7b). The ureter wall exhibited normal structure whilst no loss of transitional epithelium, indicating no epithelium lesion (Fig. 7c). The bladder wall structure appeared normal after 12 weeks implantation, and there were no inflammatory infiltrates in the outer mucosa and the muscularis (Fig. 7d).

The stenting operation slightly impacted the bladder function of the test animals. Significantly higher urinary frequency was observed in both magnesium and JQ groups during the first three weeks implantation (Fig. 8a). Significantly ($p < 0.05$) less voided volume was also observed in both magnesium group (99.7 ± 7.9 mL at 0w; 75.0 ± 15.2 mL at 3w) and JQ group (96.3 ± 9.7 mL at 0w; 78.2 ± 18.1 mL at 3w) in the first stage of implantation, and increased to normal levels from 6w post-operation (Fig. 8b). Cystometric results (Fig. 8c) revealed less negative influence on bladder functions of JQ groups than Mg groups. Higher bladder capacity (143.7 ± 21.3 mL) and starting filling pressure (15.8 ± 6.2 cm H_2O) were observed in Mg group after operation, which corresponded to elevations in post-void residual volumes. After 12 weeks implantation, no significant differences were observed in the four primary bladder function indices (bladder capacity, Qmax, starting filling pressure and ending filling pressure) between the two groups. The highest bacteria numbers in urine (73 CFUs in Mg; 62 CFUs in JQ) were observed after 6 weeks implantation, indicating that peri-implant infections occurred in the first phase of the implantation period (Fig. 8d). However, less CFUs were always detected in JQ group than Mg group due to the higher antibacterial activity brought by silver ion release [17].

The transitional epithelium cells were observed by using TEM, and the cellular components inside the cells could be clearly visualized in dark color due to their electron-dense structure (Fig. 9) [32]. In Mg group, the cells displayed regular ovoid shape nucleus. Both condensed and loose chromatin were observed dispersed in the nucleoplasmic space and attached to the inner nuclear membrane (Fig. 9a). Multiple nuclear pores and indentations in the nuclear membrane were observed. Other notable morphological features include smooth endoplasmic reticulum, rough endoplasmic reticulum, desmosomal junctions, intermediate filaments and free ribosomes. The cells in JQ group showed more compact nucleus with uniformly distributed loose chromatin (Fig. 9b). Narrow bands of condensed chromatin was observed on the inner nuclear membrane. Like Mg group, desmosomal junctions and free ribosomes could also be detected in JQ group. However, the smooth endoplasmic reticulum were better developed in JQ group than Mg group, and a decreased lamina propria widening was also observed in JQ group.

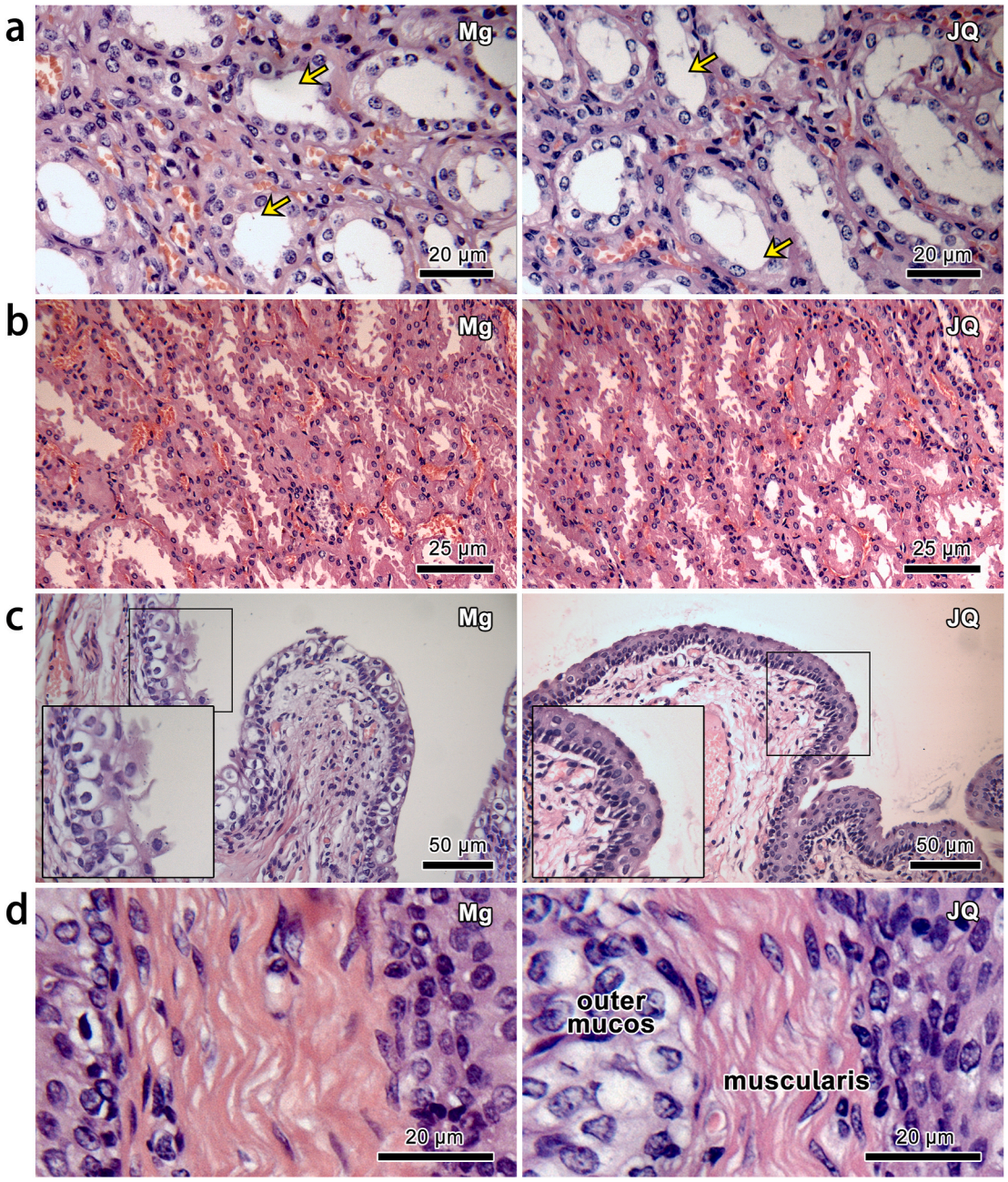

Fig. 7. Selected tissue sections (H/E stained) of the renal tubules (**a**, proximal tubule was marked with yellow arrows), the renal pelvis (**b**), the ureter (**c**, transitional epithelium was presented in larger magnification) and the bladder (**d**) of the test animals in control and test groups at 12w post-operation.

4. Discussion

Design of a ureteral stent implant plays a very important role to successfully maintain the lumen patency of the ureter [6]. Therefore, to a biodegradable ureteral stent, the primary objective is to assure sufficient mechanical properties during the whole degradation process. Among various mechanical properties, tensile strength and elongation are the most crucial parameters to determine the support performance of the stent [10,33,34]. Combining our experimental observation on the tensile behavior with the fracture morphology analysis enables to rationalize the fracture process (Fig. 3). In light of these findings, the fracture mechanism in pure magnesium and JQ alloy could be revealed as follow. In pure magnesium, micro-cracks and voids nucleated along grain boundaries. Thereafter, micro-cracks quickly grew and led to brittle intergranular fracture due to the lower elongation of pure magnesium. Attributed to the refined microstructure and small-sized second phases, ductile fracture could be observed in the tensile process of JQ alloy. Similar to pure magnesium, micro-cracks also generated along with increasing load. However, those micro-cracks further formed micro-voids and nucleated around second phases along grain boundaries. Due to the spatial arrangement of the second phases along grain boundaries, the micro-void stopped growing soon after their formation [35,36]. At this stage, triaxiality effects began to manifest as shown in the 3D reconstruction of the microstructure of the JQ alloy in Fig. 3 [37]. As a result, the brittle intergranular fracture in the early phase of the tensile process were transformed to ductile fracture process, which appropriately met the anisotropic fracture models [38]. Therefore, the improved tensile strength and elongation as well as the ductile fracture behavior of JQ together assured sufficient support performance of the stent during its whole degradation process.

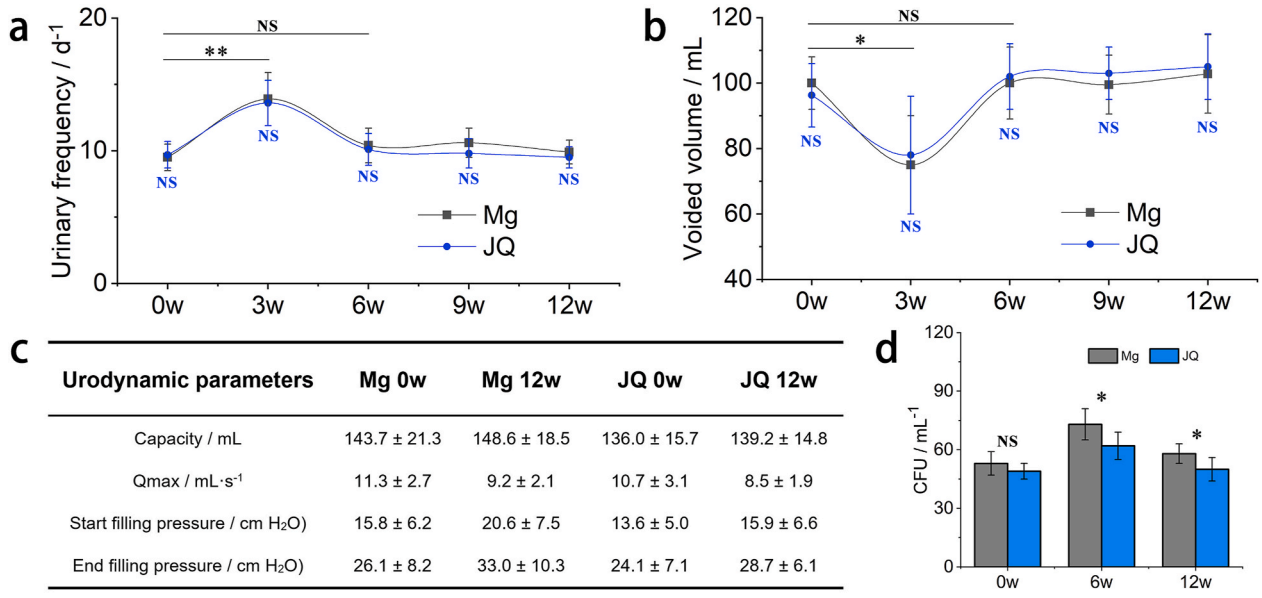

Urodynamic parameters	Mg 0w	Mg 12w	JQ 0w	JQ 12w
Capacity / mL	143.7 ± 21.3	148.6 ± 18.5	136.0 ± 15.7	139.2 ± 14.8
Qmax / mL·s^{-1}	11.3 ± 2.7	9.2 ± 2.1	10.7 ± 3.1	8.5 ± 1.9
Start filling pressure / cm H_2O)	15.8 ± 6.2	20.6 ± 7.5	13.6 ± 5.0	15.9 ± 6.6
End filling pressure / cm H_2O)	26.1 ± 8.2	33.0 ± 10.3	24.1 ± 7.1	28.7 ± 6.1

Fig. 8. The emictions conditions (**a, b**), cystometric analysis (**c**) and bacteria numbers in urine (**d**) of the experimental animals during the implantation period.

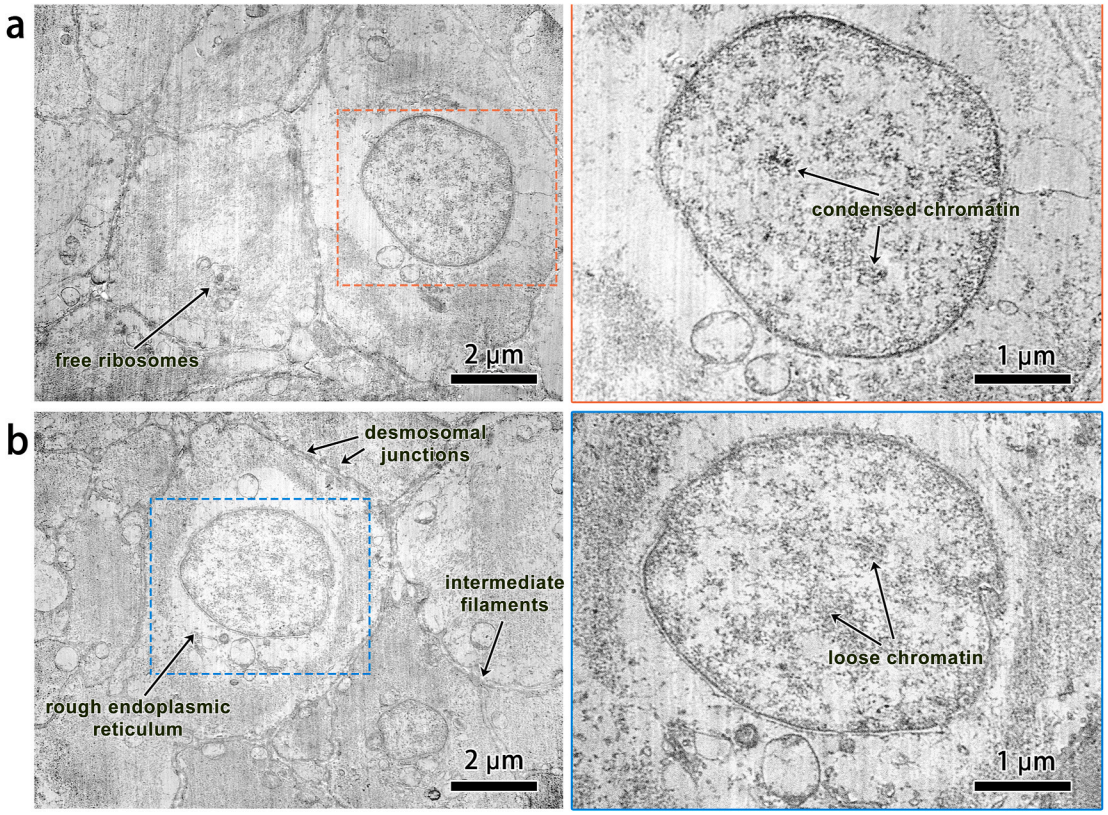

Fig. 9. Transmission electron micrographs of transitional epithelium cells from the ureter wall at the implantation sites in Mg group (**a**) and JQ group (**b**).

Biofilm formation on the surface of ureteral stents has been reported as the first step in the process of peri-implant infection [4,14,16]. As the proximate cause of peri-implant infections, bacterial colonization on biofilm was found in 24% cases in the first 4 weeks post-operation and more than 70% after 6 weeks [4]. Besides, diabetes mellitus and chronic renal failure were associated with bacteriuria caused by peri-implant infections [12]. However, routine treatment and screening were proved not effective to prevent these complications. Akay et al. [13] reported on a long-term antibiotic treatment throughout the entire implantation period, during which no significant remission of infections was observed. Indwelling time was proved the most crucial parameter to determine the biofilm formation on stents, which is found in over 75% of stenting cases at 12 weeks post-operation [15]. Consequently, the biodegradability and antibacterial activity of JQ alloy as very favorable advantages should paid special attention.

We used the number of CFUs to determine if there was bacteriuria. An order-of-magnitude reduction of CFUs is commonly necessary to prove the significant antibacterial activity *in vitro*. However, in clinical

practice, statistically significant difference in CFUs is the judging criteria of bacteriuria. Therefore, we determined the *in vivo* antibacterial activity through evaluating the risk of bacteriuria. In comparison to permanent implant materials, the constantly degrading surface of JQ alloy could completely inhibit biofilm formation, and therefore reducing most of the complications related to peri-infections [7,17]. In an examination of antimicrobial activities of biodegradable magnesium based materials, Nguyen et al. [19] identified several possible mechanisms of antimicrobial activity that may occur as a single activity or in tandem, including oxidative stress, interruption of quorum sensing processes, and changes in Ca^{2+} ion concentrations in extracellular fluids that result from the degradation of magnesium. The effects of these activities may also be dependent on the thickness of Gram-positive and Gram-negative peptidoglycan structures and the presence of an outer cell membrane in Gram-negative bacteria [20]. Additionally, although magnesium metal degradation leads to the release of hydrogen ions (H^+) into the surrounding solution, here it was shown that inhibition of bacterial growth was not a result of the effects of hydrogen ion release [19,20]. Lock et al. [21] identified a significant decrease in bacterial proliferation when magnesium alloys degraded in artificial urine. Zhang et al. [22] determined that magnesium alloy degradation produced a more significant reduction in the proliferation of Methicillin-resistant *Staphylococcus aureus* (MRSA) when the bacteria were in direct contact with alloy surfaces. In our study, apart from the contribution to antibacterial process from the a rise in pH and the Mg^{2+} ion release, the Ag^+ ion release during the degradation of JQ also played very an important role due to its strong antibacterial activity (Figs. 1 and 2) [39]. Due to this antibacterial activity, we could observe significantly less CFUs in urine (Fig. 8d), which further led to an absence of nucleus fragmentation and the recovered lamina propria compared with control group (Fig. 7).

Our findings suggest that JQ stent may as well improve the postoperative bladder functions viewed from the urodynamic results. Less negative influence on bladder functions of JQ groups than Mg groups could be concluded based on cystometric analysis (Fig. 8c). Lower bladder capacity and starting filling pressure were observed in JQ group during implantation period, indicating less post-void residual volumes due to the less peri-implant infections. Abnormal bladder functions were frequently found after ureteral implantation surgeries, among which ureteral obstruction presents an incidence more than 10% [40]. In Baumgarten et al.'s study [41], the average examined ureter passage rate of 119 cases after stenting was merely ca. 14%. Traditional permanent metallic ureteral stents can hardly get rid of the problems brought by biofilm formation due to the constant interface between stents and urine [7,10]. By contrast, magnesium ureteral stents represented by JQ stents are completely biodegradable. Like in our study, the JQ stents kept degrading during the 12 weeks implantation, which reduced the risk of urinary tract obstruction caused by biofilm formation. Additional advantages of biodegradable magnesium stents also include reducing the incidence rate of other complication like ureteral stones induced by unnecessary indwelling time [1,42]. The degradation period could be fully adjusted by tailoring the weight and surface area of the JQ stents, which makes it possible to accurately match the indwelling time with degradation period [23,43].

This primary and exploratory study represents many scientifically significant results. However, more randomized and prospective multicenter studies using multiple animal models are still needed to comprehensively testify the applicability of the alloy. Tailoring of the alloy composition, long-term experiments and comparative studies among different magnesium alloys will be the major orientations of our future study.

5. Conclusions

The biodegradable Mg-Sr-Ag alloy reported here displays its significant potential as antibacterial biodegradable ureteral stents. During the rheo-solidificaiton process, the matrix as well as the $Mg_{17}Sr_2$ and Mg_4Ag particles were fully spheroidized and refined. $Mg(OH)_2$, MgO, CaC_2O_4, $SrCl_2$ and AgCl were found in the degradation layer via XPS analysis. The ultimate tensile strength increased from 105.9 MPa in pure magnesium to 223.7 MPa in JQ alloy. *In vitro* test proved the alloy's good cytotoxicity, and blood tests towards four crucial biochemical indices revealed its excellent histocompatibility. Cystometric results revealed the less negative influence on bladder functions of JQ alloy than pure magnesium due to the higher antibacterial activity brought by silver ion release. Due to this antibacterial activity, we could observe significantly less CFUs in urine, which further led to an absence of nucleus fragmentation and recovered lamina propria. Additional advantages of the alloy also include reducing the incidence rate of other complication like ureteral stones induced by unnecessary indwelling time. These discoveries make antibacterial biodegradable metallic materials represented by JQ alloy particularly noteworthy candidates as ureteral implant materials.

CRediT authorship contribution statement

Di Tie: Conceptualization, Writing – original draft. **Norbert Hort:** Supervision. **Minfang Chen:** Formal analysis. **Renguo Guan:** Writing – review & editing. **Sviatlana Ulasevich:** Investigation, Formal analysis. **Ekaterina V. Skorb:** Investigation. **Dapeng Zhao:** Project administration. **Yili Liu:** Investigation, Data curation. **Patricia Holt-Torres:** Investigation, Data curation. **Huinan Liu:** Methodology.

Declaration of competing interest

Conflicts of interest: none.

Acknowledgement

This work was supported by National Natural Science Foundation of China (grant numbers 51771045 and U1764254). Special thanks are due to the instrumental analysis from Analytical and Testing Center, Northeastern University. The authors sincerely acknowledge the Animal Experimental Center of China Medical University for the *in vivo* experiments.

References

[1] S. Salter, A. Lee, J. Jaya, N. Suh, M.K. Yii, A. Saunder, Timely surgical intervention for ureteric complications ensures adequate graft function in renal transplantation: a 10-year review, ANZ J. Surg. 90 (7–8) (2020) 1340–1346.
[2] Y.M. Xu, C. Feng, H. Kato, H. Xie, X.R. Zhang, Long-term outcome of ileal ureteric replacement with an iliopsoas muscle tunnel antirefluxing technique for the treatment of long-segment ureteric strictures, Urology 88 (2016) 201–206.
[3] J. Kwong, D. Schiefer, G. Aboalsamh, J. Archambault, P.P. Luke, A. Sener, Optimal management of distal ureteric strictures following renal transplantation: a systematic review, Transpl. Int. 29 (5) (2016) 579–588.
[4] M. Beysens, T.O. Tailly, Ureteral stents in urolithiasis, Asian J. Urol. 5 (4) (2018) 274–286.
[5] M. Castagnetti, M. Iafrate, C. Esposito, R. Subramaniam, Searching for the least invasive management of pelvi-ureteric junction obstruction in children: a critical literature review of comparative outcomes, Front. Pediatr. 8 (2020) 6.
[6] C.C. Khoo, H. Abboudi, R. Cartwright, T. El-Husseiny, R. Dasgupta, Metallic ureteric stents in malignant ureteric obstruction: a systematic review, Urology 118 (2018) 12–20.
[7] P. Betschart, V. Zumstein, M.T. Buhmann, S. Altenried, C. Babst, G. Mullhaupt, S. Gusewell, H.P. Schmid, Q. Ren, D. Abt, Symptoms associated with long-term double-J ureteral stenting and influence of biofilms, Urology 134 (2019) 72–78.
[8] J. Fu, Y. Su, Y.-X. Qin, Y. Zheng, Y. Wang, D. Zhu, Evolution of metallic cardiovascular stent materials: a comparative study among stainless steel, magnesium and zinc, Biomaterials 230 (2020), 119641.
[9] H.B. Joshi, S.V. Chitale, M. Nagarajan, S.O. Irving, A.J. Browning, C.S. Biyani, N. A. Burgess, A prospective randomized single-blind comparison of ureteral stents composed of firm and soft polymer, J. Urol. 174 (6) (2005) 2303–2306.
[10] A. Abbasi, H.W. Wyre, K. Ogan, Use of full-length metallic stents in malignant ureteral obstruction, J. Endourol. 27 (5) (2013) 640–645.
[11] M.T. Buhmann, D. Abt, S. Altenried, P. Rupper, P. Betschart, V. Zumstein, K. Maniura-Weber, Q. Ren, Extraction of biofilms from ureteral stents for quantification and cultivation-dependent and -independent analyses, Front. Microbiol. 9 (2018).

[12] A.F. Akay, U. Aflay, A. Gedik, H. Şahin, M.K. Bircan, Risk factors for lower urinary tract infection and bacterial stent colonization in patients with a double J ureteral stent, Int. Urol. Nephrol. 39 (1) (2007) 95–98.
[13] F. Moltzahn, K. Haeni, F.D. Birkhäuser, B. Roth, G.N. Thalmann, P. Zehnder, Peri-interventional antibiotic prophylaxis only vs continuous low-dose antibiotic treatment in patients with JJ stents: a prospective randomised trial analysing the effect on urinary tract infections and stent-related symptoms, BJU Int. 111 (2) (2013) 289–295.
[14] K. Arkusz, K. Pasik, A. Halinski, A. Halinski, Surface Analysis of Ureteral Stent before and after Implantation in the Bodies of Child Patients, Urolithiasis, 2020.
[15] T. Kawahara, H. Ito, H. Terao, M. Yoshida, J. Matsuzaki, Ureteral stent encrustation, incrustation, and coloring: morbidity related to indwelling times, J. Endourol. 26 (2) (2011) 178–182.
[16] X.P. Li, H. Gao, X.L. Sun, Z.X. Huang, B. Wang, Y. Li, W. Wei, C.J. Wang, Y.L. Ni, A preliminary study on the role of Bacteroides fragilis in stent encrustation, World J. Urol. 10.
[17] D. Tie, F. Feyerabend, W.-D. Mueller, R. Schade, K. Liefeith, K.U. Kainer, R. Willumeit, ANTIBACTERIAL BIODEGRADABLE Mg-Ag ALLOYS, Eur. Cell. Mater. 25 (2013) 284–298.
[18] S. Wang, X.Q. Zhang, J.G. Li, C.S. Liu, S.K. Guan, Investigation of Mg-Zn-Y-Nd alloy for potential application of biodegradable esophageal stent material, Bioact. Mater. 5 (1) (2020) 1–8.
[19] N.T. Nguyen, N. Grelling, C.L. Wetteland, R. Rosario, H. Liu, Antimicrobial activities and mechanisms of magnesium oxide nanoparticles (nMgO) against pathogenic bacteria, yeasts, and biofilms, Sci. Rep. 8 (1) (2018), 16260.
[20] C.L. Wetteland, J. de Jesus Sanchez, C.A. Silken, N.-Y.T. Nguyen, O. Mahmood, H. Liu, Dissociation of magnesium oxide and magnesium hydroxide nanoparticles in physiologically relevant fluids, J. Nanoparticle Res. 20 (8) (2018) 215.
[21] J.Y. Lock, E. Wyatt, S. Upadhyayula, A. Whall, V. Nuñez, V.I. Vullev, H. Liu, Degradation and antibacterial properties of magnesium alloys in artificial urine for potential resorbable ureteral stent applications, J. Biomed. Mater. Res. 102 (3) (2014) 781–792.
[22] C. Zhang, J. Lin, N.-Y.T. Nguyen, Y. Guo, C. Xu, C. Seo, E. Villafana, H. Jimenez, Y. Chai, R. Guan, H. Liu, Antimicrobial bioresorbable Mg–Zn–Ca alloy for bone repair in a comparison study with Mg–Zn–Sr alloy and pure Mg, ACS Biomater. Sci. Eng. 6 (1) (2020) 517–538.
[23] D. Tie, R. Guan, H. Liu, A. Cipriano, Y. Liu, Q. Wang, Y. Huang, N. Hort, An in vivo study on the metabolism and osteogenic activity of bioabsorbable Mg-1Sr alloy, Acta Biomater. 29 (2016) 455–467.
[24] D. Tie, B. Zhang, L. Yan, R. Guan, Z. Ji, H. Liu, D. Zhang, D. Liu, M. Chen, Rheological solidification behavior and mechanical properties of AZ91-Sn alloys, Crystals 9 (12) (2019).
[25] Y.F. Shen, R.G. Guan, Z.Y. Zhao, R.D.K. Misra, Ultrafine-grained Al–0.2Sc–0.1Zr alloy: the mechanistic contribution of nano-sized precipitates on grain refinement during the novel process of accumulative continuous extrusion, Acta Mater. 100 (2015) 247–255.
[26] ASTM, Standard Practice for Codification of Certain Nonferrous Metals and Alloys, B275, Cast and Wrought, 2013.
[27] D. Tie, R. Guan, H. Liu, A. Cipriano, Y. Liu, Q. Wang, Y. Huang, N. Hort, An in vivo study on the metabolism and osteogenic activity of bioabsorbable Mg–1Sr alloy, Acta Biomater. 29 (2016) 455–467.
[28] A. Kula, C.J. Silva, M. Niewczas, Grain size effect on deformation behaviour of Mg–Sc alloys, J. Alloys Compd. 727 (2017) 642–657.
[29] Y. Sun, H.L. Wu, W.H. Wang, R. Zan, H.Z. Peng, S.X. Zhang, X.N. Zhang, Translational status of biomedical Mg devices in China, Bioact. Mater. 4 (2019) 358–365.
[30] D. Kishawi, G. Schwarzman, A. Mejia, A.K. Hussain, M.H. Gonzalez, Low preoperative albumin levels predict adverse outcomes after total joint arthroplasty, J. Bone Joint Surg.-Am. 102 (10) (2020) 889–895.
[31] D. Tie, H. Liu, R. Guan, P. Holt-Torres, Y. Liu, Y. Wang, N. Hort, In vivo assessment of biodegradable magnesium alloy ureteral stents in a pig model, Acta Biomater. 116 (2020) 415–425.
[32] T. Okumura, M. Shoji, A. Hisada, Y. Ominami, S. Ito, T. Ushiki, M. Nakajima, T. Ohshima, Electron tomography of whole cultured cells using novel transmission electron imaging technique, Micron 104 (2018) (1993) 21–25. Oxford, England.
[33] J. Asakawa, T. Iguchi, S. Tamada, N. Ninomiya, M. Kato, T. Yamasaki, T. Nakatani, Outcomes of indwelling metallic stents for malignant extrinsic ureteral obstruction, Int. J. Urol. 25 (3) (2018) 258–262.
[34] J. Asakawa, T. Iguchi, S. Tamada, N. Ninomiya, M. Kato, T. Yamasaki, T. Nakatani, Treatment outcomes of ureteral stenting for malignant extrinsic ureteral obstruction: a comparison between polymeric and metallic stents, Canc. Manag. Res. 10 (2018) 2977–2982.
[35] Z. Wang, S. Yao, G. Cao, P. Mao, F. Wang, L. Zhou, Z. Liu, Effect of yttrium addition on dynamic mechanical properties, microstructure, and fracture behavior of extrusion-shear ZC61 + xY (x = 0, 1, 2, 3) alloys, Mater. Char. 169 (2020), 110615.
[36] R. Sarvesha, W. Alam, A. Gokhale, T.S. Guruprasad, S. Bhagavath, S. Karagadde, J. Jain, S.S. Singh, Quantitative assessment of second phase particles characteristics and its role I on the deformation response of a Mg-8Al-0.5Zn alloy, Mater. Sci. Eng. A-Struct. Mater. Prop. Microstruct. Process. 759 (2019) 368–379.
[37] B. Kondori, A.A. Benzerga, Effect of stress triaxiality on the flow and fracture of Mg alloy AZ31, Metall. Mater. Trans. 45 (8) (2014) 3292–3307.
[38] B. Kondori, A.A. Benzerga, Modeling damage accumulation to fracture in a magnesium-rare earth alloy, Acta Mater. 124 (2017) 225–236.
[39] V. Bundjaja, S.P. Santoso, A.E. Angkawijaya, M. Yuliana, F.E. Soetaredjo, S. Ismadji, A. Ayucitra, C. Gunarto, Y.-H. Ju, M.-H. Ho, Fabrication of cellulose carbamate hydrogel-dressing with rarasaponin surfactant for enhancing adsorption of silver nanoparticles and antibacterial activity, Mater. Sci. Eng. C 118 (2021), 111542.
[40] A. Breda, M.H. Bui, J.C. Liao, H.A. Gritsch, P.G. Schulam, Incidence of ureteral strictures after laparoscopic donor nephrectomy, J. Urol. 176 (3) (2006) 1065–1068.
[41] L. Baumgarten, A. Desai, S. Shipman, D.D. Eun, M.A. Pontari, J.H. Mydlo, A. C. Reese, Spontaneous passage of ureteral stones in patients with indwelling ureteral stents, Can. J. Urol. 24 (5) (2017) 9024–9029.
[42] S. Adanur, F. Ozkaya, Challenges in treatment and diagnosis of forgotten/encrusted double-J ureteral stents: the largest single-center experience, Ren. Fail. 38 (6) (2016) 920–926.
[43] C. Li, C. Guo, V. Fitzpatrick, A. Ibrahim, M.J. Zwierstra, P. Hanna, A. Lechtig, A. Nazarian, S.J. Lin, D.L. Kaplan, Design of biodegradable, implantable devices towards clinical translation, Nat. Rev. Mater. 5 (1) (2020) 61–81.